Remote Sens. **2014**, *6*, 4149-4172; doi:10.3390/rs6054149

OPEN ACCESS

remote sensing

ISSN 2072-4292

www.mdpi.com/journal/remotesensing

Article

Determination of Carbonate Rock Chemistry Using Laboratory-Based Hyperspectral Imagery

Nasrullah Zaini [1,2,*], Freek van der Meer [1] and Harald van der Werff [1]

[1] Department of Earth Systems Analysis, Faculty of Geo-Information Science and Earth Observation (ITC), University of Twente, P.O. Box 217, 7500 AE Enschede, The Netherlands; E-Mails: f.d.vandermeer@utwente.nl (F.M.); harald.vanderwerff@utwente.nl (H.W.)

[2] Department of Physics, Faculty of Mathematics and Natural Sciences, Syiah Kuala University, Darussalam, Banda Aceh, 23111 Aceh, Indonesia

* Author to whom correspondence should be addressed; E-Mail: n.zaini@utwente.nl; Tel.: +31-534-874-444; Fax: +31-534-874-400.

Received: 6 December 2013; in revised form: 11 April 2014 / Accepted: 28 April 2014 / Published: 5 May 2014

Abstract: The development of advanced laboratory-based imaging hyperspectral sensors, such as SisuCHEMA, has created an opportunity to extract compositional information of mineral mixtures from spectral images. Determining proportions of minerals on rock surfaces based on spectral signature is a challenging approach due to naturally-occurring minerals that exist in the form of intimate mixtures, and grain size variations. This study demonstrates the application of SisuCHEMA hyperspectral data to determine mineral components in hand specimens of carbonate rocks. Here, we applied wavelength position, spectral angle mapper (SAM) and linear spectral unmixing (LSU) approaches to estimate the chemical composition and the relative abundance of carbonate minerals on the rock surfaces. The accuracy of these classification methods and correlation between mineral chemistry and mineral spectral characteristics in determining mineral constituents of rocks are also analyzed. Results showed that chemical composition (Ca-Mg ratio) of carbonate minerals at a pixel (e.g., sub-grain) level can be extracted from the image pixel spectra using these spectral analysis methods. The results also indicated that the spatial distribution and the proportions of calcite-dolomite mixtures on the rock surfaces vary between the spectral methods. For the image shortwave infrared (SWIR) spectra, the wavelength position approach was found to be sensitive to all compositional variations of carbonate mineral mixtures when compared to the SAM and LSU approaches. The correlation between geochemical elements and spectroscopic parameters also revealed the presence of

these carbonate mixtures with various chemical compositions in the rock samples. This study concludes that the wavelength position approach is a stable and reproducible technique for estimating carbonate mineral chemistry on the rock surfaces using laboratory-based hyperspectral data.

Keywords: SisuCHEMA hyperspectral data; carbonate rocks; mineral mixtures; SWIR reflectance spectra; spectral recognition approaches; geochemical analysis

1. Introduction

Carbonate rocks are one of the important and abundant constituents of materials on the earth surface. This is because the rocks not only possess natural resources, such as valuable minerals and including fossil fuels, but also contain history of the earth surface environments in the past [1,2]. Thus, identification and quantification of the abundances and proportions of carbonate minerals on the rock surfaces is essential for minerals exploration and understanding petroleum geology characterization. The rocks are constituted by a mosaic of minerals and naturally complex geologic mixtures, such as intimate mixtures, grain size variations, weathered constituents, and alteration products [1,2]. Those mixtures can create a major obstacle to mineralogic identification [3–5], particularly determining the proportions of mineral mixtures. Conventional methods to identify carbonate minerals in rock samples include X-ray diffraction (XRD) [6–9], scanning electron microscopy (SEM) [7,10], different thermal analysis (DTA) [7], thin section analysis [11,12], staining method [13–16], and others. However, most of these methods incur costly techniques and time consuming in terms of sample preparation and analysis. A promising approach, which is fast, inexpensive, non-destructive and can achieve a higher degree of accuracy in identification and estimation of the abundance of carbonate mineral mixtures, is hyperspectral imaging spectroscopy techniques.

The recent developments of laboratory-based imaging spectrometry sensors such as HyLogging™, HySpex, SisuROCK, and SisuCHEMA hyperspectral imagers, which integrated the sophisticated digital imaging of airborne hyperspectral sensor technologies with the highest spectroscopic resolution of field and laboratory spectrometers, have generated a new type of hyperspectral imagery that can be used for identifying geologic mixtures of surface mineralogy [17–21]. These spectrometers can acquire hyperspectral images of powdered or hand specimen samples for a wide variety of applications including chemical imaging, pharmaceutical, and mineralogical identification. These relatively novel datasets present new opportunities for analysis of the complex mixtures of surface mineralogy. However, the datasets have not been fully explored in determining mineral mixtures and estimating the proportions of these minerals on a hand specimen of rock or geologic sample [18,20]. Therefore, the application of higher resolution hyperspectral imagery that enables the determination of the abundance of naturally mixed minerals on rock surfaces is still challenging.

This analysis uses higher resolution hyperspectral imagery of the SisuCHEMA hyperspectral scanner to determine and estimate the abundance of mineral mixtures on hand specimens of fresh carbonate rock surfaces. It is also complemented by geochemical analysis of spot measurements obtained by a portable X-ray fluorescence (PXRF) analyzer for identifying mineral chemistry of the

rocks. The spectrometer, which was originally designed for chemical imaging, is an automatic hyperspectral imaging instrument for rapid scanning and analysis of various samples in laboratory [17]. It acquires imagery of the sample mounted on its imaging tray using a push-broom hyperspectral sensor. The instrument can be equipped with a shortwave infrared (SWIR) sensor. In this regard, the higher resolution SisuCHEMA imagery provides an additional spatial detail to spectral information of surface feature characteristics in image pixels. It allows further determination of mineral assemblages or mixtures and estimation of the relative mineral abundances on the carbonate rock surfaces using various spectral recognition algorithms.

In order to extract compositional information of mineralogy based on their spectral characteristics in hyperspectral imaging data, a number of well-developed spectral classification approaches are commonly used. These consist of wavelength position analysis [5,22,23], spectral angle mapper (SAM) [24], and linear spectral unmixing (LSU) [25,26]. The approaches have various advantages of spectral classification algorithms, as well as relatively accurate methods in identifying minerals from image spectra. These methods have also been used extensively for mapping surface mineralogy of hyperspectral data in different geological samples or areas [5,18,20,24,27–30]. Wavelength position analysis approach is sensitive to band position shift and noisier spectral responses [20,23], which is determined from a polynomial fit [23] of continuum-remove spectra [5,22]. SAM, a spectral similarity measure [24], is insensitive to illumination and albedo differences [27–29,31]. LSU provides an interesting alternative approach to mixing problem of pixel spectra [25,26]. It can derive fractional abundances for selected endmembers within a pixel. Thus, detection of the exact absorption wavelength position and unique spectral shape is a key factor for direct identification of surface mineralogy [5,32–35].

The SWIR reflectance spectra (1.0–2.5 μm) are rich in mineral spectral signatures. Within this spectral range, the diagnostic absorption features are determined by the occurrence of water (H_2O), hydroxyl (OH), carbonate (CO_3), and sulfate (SO_4) [32–35]. Spectral absorption feature characteristics of minerals vary, depending on the chemical composition, structural arrangement, and bonding characteristics [4,36,37]. Hence, these feature characteristics can be used for discriminating one mineral from the other. Carbonate minerals, such as calcite ($CaCO_3$) and dolomite ($CaMg(CO_3)_2$), are the most common constituents of carbonate rocks [1,2]. They have two prominent absorption features in the SWIR region centered within the wavelength ranges of 2.530–2.541 μm and 2.333–2.340 μm and 2.503–2.520 μm and 2.312–2.323 μm, respectively [8,18,32,34,37–40]. Those absorption features are caused by vibrational processes of the carbonate ions (CO_3^{2-}) [8,32,34]. Moreover, the positions of absorption features of calcite-dolomite mixtures in the SWIR region were determined by the calcite or dolomite content in the carbonate samples [37,38]. Absorption feature characteristics of these minerals are also influences by particle size [8,37–39], texture [39], porosity [8], and mineral impurities [8,37,39]. The presence of clay minerals in intimate mixture with carbonates is usually indicated by a vibrational absorption feature around 2.20 μm and 2.30 μm due to the combination of the OH stretch with the Al-OH and Mg-OH bending modes, respectively [33–35].

The objectives of this study are to (i) estimate the chemical composition and the relative abundance of carbonate minerals on the rock surfaces using wavelength position, SAM and LSU approaches, (ii) assess the accuracy of these classification methods for identification of surface mineralogy, and (iii) find relationship between mineral chemistry and mineral spectral characteristics in determining

mineral constituents of rocks. The advent of higher resolution hyperspectral data provided by the SisuCHEMA SWIR sensor could potentially help to solve the problem of determining the relative abundance of mineral mixtures composing rocks or geologic samples.

2. Materials and Methods

2.1. SisuCHEMA Hyperspectral Data

The data used in this study were higher resolution hyperspectral imagery of carbonate rocks acquired by the SisuCHEMA hyperspectral imager of Spectral Imaging Ltd. (SPECIM), Finland [17]. We used the SWIR hyperspectral sensor, which acquires images with 320 spatial pixels per line at a spatial resolution of 0.21 mm. The imaging sensor is configured to record continuous spectral information from 970 nm to 2500 nm with 256 spectral bands at an average full width at half maximum (FWHM) of 6.23 nm and spectral resolution of 10 nm [17]. Samples are scanned on a moving imaging tray under similar illumination conditions by using SPECIM's diffused line illumination unit. The scanner is integrated with a computer workstation as shown in Figure 1 taken from Agus [41] that allows acquiring and saving spectral image in real-time using the ChemaDAQ data acquisition software. An internal standard reference target is used for calibration measurement before each sample scan. It results in automatically calibrated image data to reflectance. Its higher spatial and spectral resolution allows the SisuCHEMA to record distinctive spectral absorption features in the SWIR wavelength region, which can be applied to study mineralogical components on rock or geological surfaces.

Figure 1. An integrated system of SisuCHEMA hyperspectral scanner [41].

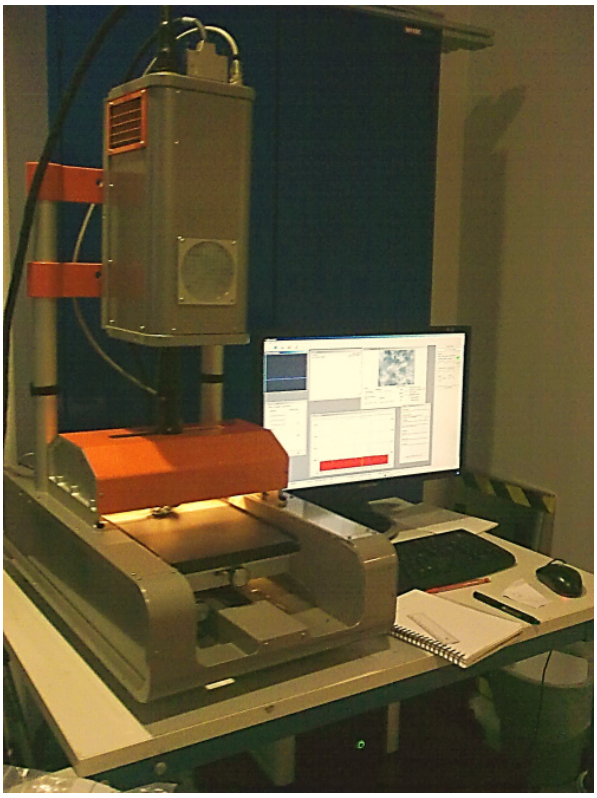

Figure 2. Fresh surfaces of carbonate rock samples, with red rectangles pointing out areas of selected SisuCHEMA images.

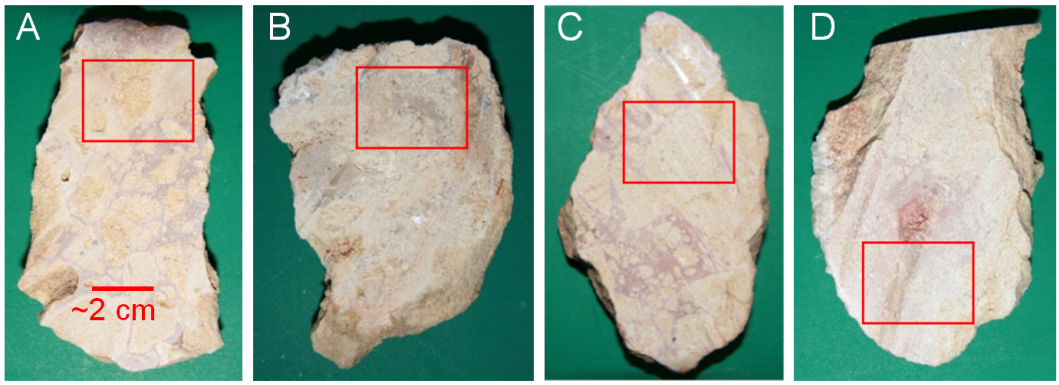

Figure 3. Selected SisuCHEMA images A, B, C, and D of carbonate rocks (bands 200, 205, and 210) with locations of two portable X-ray fluorescence (PXRF) spot measurements (red circles).

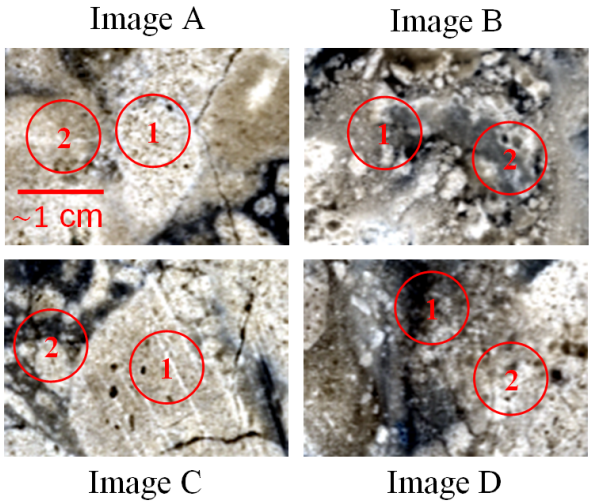

The rocks imaged were hand specimens of fresh carbonate rock surfaces (Figure 2). These rocks were collected from the Bédarieux mining area, which is an open and partly active dolomite mine in the Hérault department of Languedoc-Roussillon region, southern France. The samples are originating from the Jurrassic-Bathomien formation and their composition becomes sandier from west to east [42]. A total of four rock samples (samples A, B, C, and D) were imaged, referred to as images A, B, C, and D. These rocks were chosen and assessed visually based on the physical appearance of their carbonate mineral compositions. For the purposes of this study, the spatial and spectral subset hyperspectral images of carbonate rocks (Figure 3), with 15,756 spatial pixels (156 samples–101 lines) selected carefully over a smooth area of the rock surfaces (red rectangles, Figure 2), and a spectral range between 2100 nm and 2400 nm (Figure 4), were used. The ENVI software package version 4.7 [43] was used to process the images.

Figure 4. Example of SisuCHEMA spectra (**right**) of calcite (red curve), dolomite (blue curve) and calcite-dolomite mixtures (black curve) derived from different pixel locations of image D (**left**). The curves show shift in wavelength position of carbonate absorption feature.

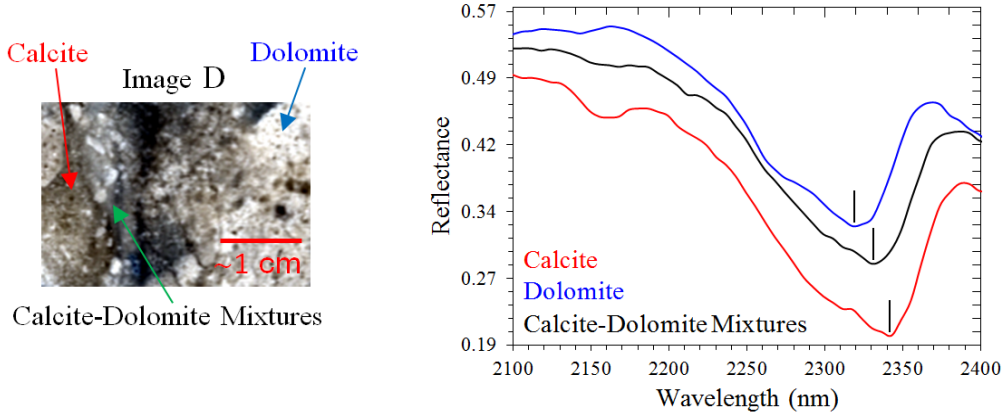

2.2. PXRF Geochemical Analysis

The major and minor element concentrations of collected carbonate rock samples were measured using a portable X-ray fluorescence (PXRF), the Niton XL3t GOLDD+ from Thermo Fisher Scientific Inc. The PXRF was also equipped with a CCD camera for accurate positioning and documenting the measurement spots. This instrument offers a rapid and non-destructive measurement for determining and investigating elemental concentrations on rocks or geologic samples [44]. For analyzing geologic samples, the analyzer was set up using mining mode option to operate excitation filters that optimize the analyzers' sensitivity for various elements. The "High Range" filter is used to optimize Ba through Ag. The "Main Range" filter provides optimum sensitivity for the elements Mn through Bi. The "Low Range" filter is used to optimize the sensitivity for the elements from Ti to Cr. The "Light Range" filter is available only with He-purged [44]. Helium purge is required to enhance detection and the quality of measurement of light elements from Mg to Cl.

Table 1. Elemental concentrations of the rock samples derived from portable X-ray fluorescence (PXRF) spot measurements (in percent). Some elements have lower limits of detection (LOD).

PXRF Spots Code	Ca	Mg	Ba	Fe	K	Al	Si	Cl	S
A1	24.47	6.54	0.02	0.08	<LOD	0.09	0.22	0.02	0.08
A2	31.66	7.10	0.03	0.07	<LOD	0.08	0.13	<LOD	0.04
B1	35.05	4.56	0.02	0.03	<LOD	<LOD	0.11	<LOD	0.04
B2	31.96	4.90	0.02	0.01	<LOD	0.08	0.11	0.04	0.02
C1	26.13	7.95	0.02	0.01	<LOD	0.07	0.18	0.05	0.11
C2	30.65	6.79	0.02	0.08	<LOD	0.10	0.16	0.05	0.03
D1	34.66	5.50	0.02	0.10	0.03	2.31	2.58	0.07	0.02
D2	31.51	7.43	0.03	0.03	<LOD	0.51	0.63	0.06	0.07

Samples in the laboratory were placed on a sample compartment over the window frame of the sensor. Two PXRF spot measurements with an 8 mm diameter spot size were taken from each fresh

carbonate rock surface within the selected area of SisuCHEMA images (Figure 3). The PXRF in mining mode setting is calibrated for a silicate dominated rock matrix. Some pure carbonate samples were analyzed to check the calibration in this mode and an over estimation of up to 10% was observed for Ca and Mg. As the samples used in this research consist of a mixture of calcite and dolomite, the last of which the Ca/Mg proportion is not known, it was not possible to establish a correction factor for these elements in the PXRF results. It is assumed that the measured Ca and Mg concentrations are proportionally correct. The lower limits of detection were approximately less than 0.02% for elements K, Al, and Cl (Table 1).

2.3. Spectral Classification Approaches of the SisuCHEMA Imagery

2.3.1. Laboratory Spectral Endmembers

In image classification and compositional identification of hyperspectral remotely sensed data, image pixels represented by reflectance spectra of exhibited surface mineralogy are classified on the basis of reference spectra or known spectral endmembers of minerals [5]. These endmembers are derived from field or laboratory spectra or the purest spectral image pixels or from published standard spectral libraries [24,45]. For classification of the selected SisuCHEMA images, we used pure and mixed laboratory spectral endmembers of powdered calcite and dolomite synthetic samples in the wavelength range of 2100 to 2400 nm with grain size fractions between 125 µm and 500 µm (Figure 5). The synthetic sample preparations and spectral measurements of the pure and physical mixed calcite and dolomite were essentially those described by Zaini *et al.* [38]. The carbonate compositions of these calcite-dolomite mixture spectral endmembers were ranging from pure calcite to pure dolomite. The spectra and absorption feature characteristics from these laboratory synthetic samples [38] were also used in the spectral absorption feature analysis, and compositional mineral quantification of the images by identifying absorption wavelength position of the spectral image pixels.

Figure 5. Laboratory spectral endmembers of (**a**) pure and (**b**) mixed calcite and dolomite synthetic samples (C = calcite and D = dolomite, prefix numbers showing the mineral contents in percent) (Modified after Zaini *et al.* [38]).

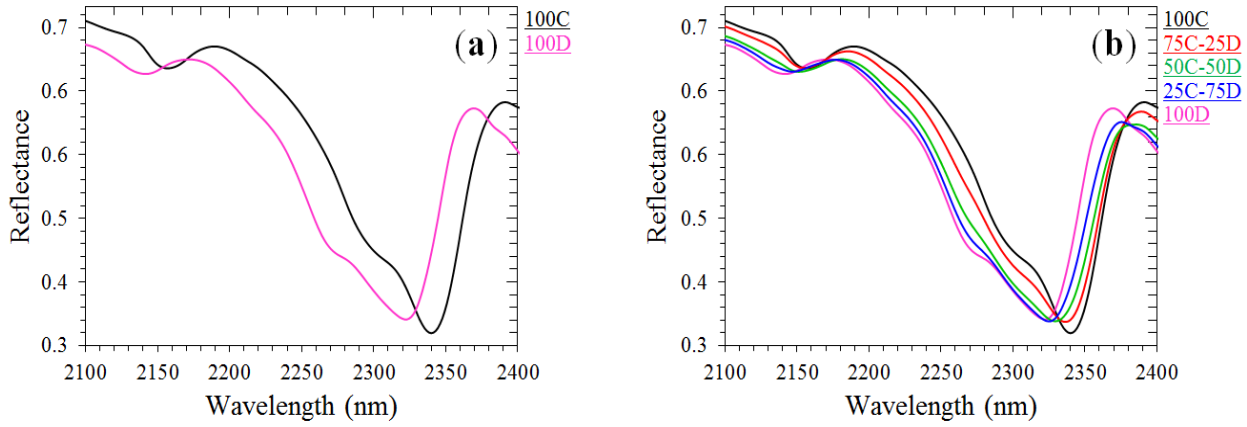

2.3.2. Absorption Wavelength Position

Mineral reflectance spectra in the SWIR wavelength region contain a number of diagnostic absorption features, which are essential for compositional quantifying and distinguishing surface mineralogy. As absorption wavelength position of spectral features of minerals exhibits distinctive characteristics of their chemical compositions and molecular bonds [4]. The absorption wavelength position calculated from continuum-removed spectra [5,22] is defined as the wavelength at which the maximum absorption or minimum reflectance of an absorption feature occurred [5,37]. The detail illustration of absorption feature characteristic definitions is given in previous studies [5,38].

In order to determine the relative abundances of mineral mixtures on the selected SisuCHEMA imagery using wavelength position analysis approach, the hyperspectral imagery was processed using Hyperspectral Python (HypPy) software package version 2.6 [46] through the following procedures. Firstly, we followed a method developed by Rodger *et al.* [23] to calculate wavelength position of a prominent absorption feature in image spectra within the wavelength range of 2100 to 2400 nm. A continuum removal was then applied to the spectra within the selected wavelength range and followed by interpolation. A second order polynomial fit is modeled to three data points of minimum reflectance in the continuum-removed spectra. The wavelength position of the minimum and depth of absorption feature was determined on the fitting polynomial curve or the resulting interpolated parabola. This process produced an image with two bands for every pixel consisted of the interpolated wavelength position of the minimum of the prominent absorption feature and the depth of the feature, respectively. The wavelength position image of band one was used to derive wavelength position of mineralogy on the image pixels. Finally, the proportion or percentage estimation of carbonate mineral mixtures on the classified wavelength position image was counted manually. It was calculated by dividing the number of pixels of each mineral class by the total number of pixels in the image and then multiplied by a hundred.

2.3.3. Spectral Angle Mapper

Spectral Angle Mapper (SAM) is a spectral matching approach that compares the spectral similarity between reflectance spectra from image pixels and reference reflectance spectra with known material constituents [24]. The spectral similarity is measured by calculating the angle between these spectra, which are characterized as vectors in space with n-dimensions equal to the number of bands. The angle of spectral vectors indicates a match of these spectra, where a smaller angle represents a closer match to the reference spectra. SAM only considers the vector directions in comparison of these spectral vectors, not their vector lengths, which are insensitive to illumination and albedo differences [24,27–29,31]. Although SAM algorithm has been widely used for classifying surface mineralogy of hyperspectral imagery in various environmental and geological conditions [18,27–30], its dependency on average match of the entire reference spectra has leaded to a certain extent of ambiguity in classification results [28,29].

SAM classification was performed for the selected SisuCHEMA images of the fresh rock surfaces with a spectral subset of 2100 to 2400 nm using the laboratory spectra of calcite-dolomite mixtures of synthetic samples [38] as endmembers with known mineralogical compositions (Figure 5b). The maximum angle used in the classification, such as single value or multiple values assigned to each spectral endmember of dataset, was defined by user in order to determine a closer match between the

endmember spectral vectors and the image pixel vectors. We performed two SAM classifications with a value of 0.1 and 0.2 (in radians), which was used as a threshold angle for each laboratory spectral endmember. ENVI basic statistics showed the percentage estimation of mineral abundances or proportions of carbonate mineral mixtures of each classified endmember in the classified image.

2.3.4. Linear Spectral Unmixing

Linear Spectral Unmixing (LSU) is a sub-pixel model algorithm assuming the reflectance at each pixel of the image to be a linear combination of the reflectance of each material (or spectral endmember) present within the pixel [25,26]. LSU uses the spectral characteristics of materials for determining the relative abundances of materials depicted in multispectral or hyperspectral imagery. But the number of endmembers used in this classification method must not be more than the number of spectral bands [25,26]. Based on user-selected spectral endmember materials extracted directly from the image or standard library, the proportional fraction of the pixel that contains the endmember material corresponding to the image was calculated using least squares techniques [47]. Thus, the approach can estimate the abundance values of each endmember for every pixel.

The unmixing algorithm was run for the selected SisuCHEMA images with a spectral subset of 2100 to 2400 nm using the laboratory spectral endmembers of the pure carbonate synthetic samples [38] (Figure 5a) to quantify carbonate mineral compositions on the hand specimens of carbonate rocks. A unit sum unconstrained and constrained unmixing was applied to classify these hyperspectral images. In the constrained method, we defined the weight of a sum-to-unity constraint on the abundance fractions with a default value of 1.0. The results of the unmixing classification were generally presented as grey-scale images with values from 0.0 to 1.0. The pixels with values of 0.0 were displayed as pure black, whereas the pixels with values of 1.0 were displayed as pure white representing higher mineral abundances and a perfect match to the endmember. The pixels having values above 1.0 or below 0.0 indicated the reference endmembers used for the classification were probably poor match, or other endmembers have to be included in the analysis [43]. ENVI classification results also produce an RMS error image that can be used to evaluate pixels of omitted or incorrect endmembers. The proportion or percentage estimation of carbonate mineral mixtures on the classified unmixing image was calculated manually. It was computed by dividing the number of pixels having the same fraction value by the total number of pixels in the image and then multiplied by a hundred.

3. Results

3.1. Identification of Carbonate Mineral Mixtures

To identify carbonate mineral mixtures and estimate the relative mineral abundances on the fresh carbonate rock surfaces, three spectral analysis techniques, such as absorption wavelength position, SAM, and LSU, have been applied to the SisuCHEMA hyperspectral images. The results in the following subsections show the relative abundances and distributions of mineral surface components estimated using these spectral methods. Generally, classification results indicate that samples B and D are composed of more heterogeneous carbonate mineral mixtures than samples A and C (Figures 6–8).

3.1.1. Wavelength Position Classification Results

Figure 6a shows variation distributions and abundances of carbonate mineral mixtures on the four carbonate rock surfaces classified by analyzing absorption wavelength positions in the SWIR spectra (2100–2400 nm) of the selected SisuCHEMA images. Absorption feature analysis of the spectral image pixels indicates that images A and C are formed mainly of dolomite (blue pixels (100D), Figure 6a); while images B and D are constituted predominantly of calcite-dolomite mixtures with different compositions of carbonate mineral contents (green (25C-75D), yellow (50C-50D) and red (75C-25D) pixels, Figure 6a). Wavelength position of dolomite (100D) is centered within the range of 2313–2323 nm. Absorption wavelength positions for various compositions of calcite-dolomite mixtures are centered within the range of 2324–2327 nm, 2328–2333 nm, and 2334–2337 nm for 25% calcite-75% dolomite (25C-75D), 50% calcite-50% dolomite (50C-50D), and 75% calcite-25% dolomite (75C-25D) mixtures, respectively. Calcite (100C) represented by cyan color in the classified images B and D (Figure 6a) is distinguished from dolomite by the presence of a carbonate feature within the wavelength range of 2338–2341 nm.

Figure 6. (**a**) Wavelength position images, showing the variability carbonate mineral mixtures. (**b**) Estimated proportion of classified minerals derived from the images. (C = calcite and D = dolomite, prefix numbers showing the mineral contents in percent).

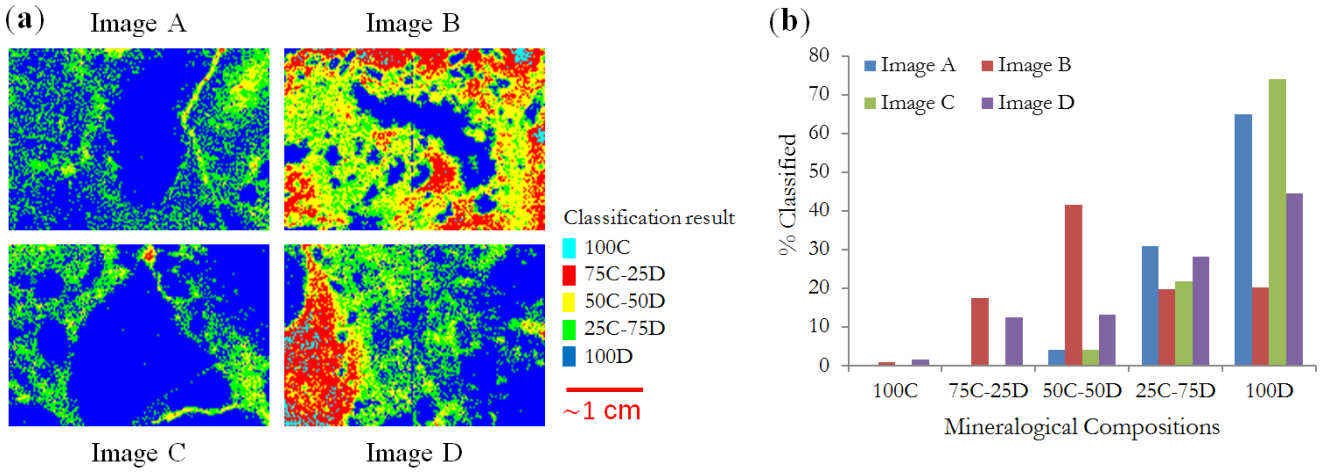

The proportion estimation of carbonate mineral mixtures composing the rock samples based on the wavelength position analysis is shown in Figure 6b. It is obvious that the classified images of the rock samples are constituted by different proportions of carbonate mineral compositions. The wavelength position image A is dominated by abundant 100D of 64.94% and abundant 25C-75D of 30.80%. The classified image B is dominated by 50C-50D with the relative mineral abundances of 41.50% and also contains small abundances of 100C of 0.94%. The relative mineral abundance estimation of image C is almost the same as the image A, where abundant 100D dominates the sample with a proportion of 73.97%. The classified image D is dominated by abundant 100D of 44.48% and abundant 25C-75D of 28.24% and also contains small abundances of 100C of 1.66%.

3.1.2. SAM Classification Results

The classified SisuCHEMA images of the rock samples resulting from the SAM algorithm using the laboratory endmembers of mixed carbonate synthetic samples [38] and a 0.1 and 0.2 radians threshold are shown in Figure 7a,c. The SAM abundance images for both threshold angles illustrate the same overall spatial distribution of carbonate minerals and slightly different proportions of these mineral mixtures due to more unclassified pixels in the SAM images of 0.1 threshold angle. Some carbonate mineral mixtures distributed over the image pixels are unclassified for both approaches (Figure 7a,c), such as the relative small abundances of 100C in the images B and D.

Figure 7. SAM classification results: (**a**) SAM images using a 0.1 radians threshold angle, (**b**) estimated proportion of classified minerals derived from (a) images, (**c**) SAM images using a 0.2 radians threshold angle, (**d**) estimated proportion of classified minerals derived from (c) images. The classification images illustrate roughly similar carbonate mineral abundances in different threshold angles. (C = calcite and D = dolomite, prefix numbers showing the mineral contents in percent).

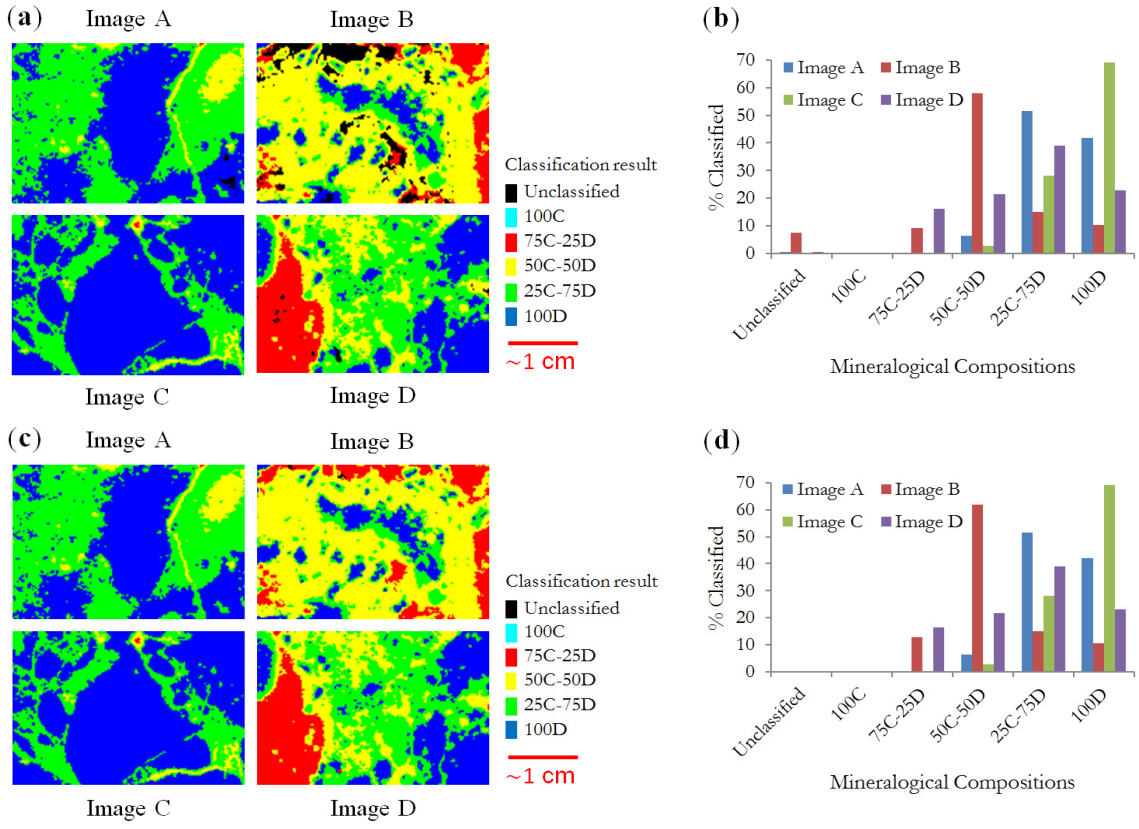

Figure 7b,d shows proportion estimation of carbonate mineral mixtures on the rock samples using the SAM classification method for different threshold angles. These graphs illustrate that the relative abundance of carbonate minerals in the resulting images slightly increase with increasing threshold angle from 0.1 to 0.2 radians. It is caused by increasing the number of classified pixels in the images. The abundance images A are dominated mostly by abundant 25C-75D of 51.61% and abundant 100D with a slight different proportion which is of 41.74% in the 0.1 threshold image and 42.09% in the 0.2 threshold image. The classified images B show the same dominant abundant 50C-50D composing the

sample, but the proportions of this carbonate mineral are 58.12% in the 0.1 threshold image and 61.77% in the 0.2 threshold image due to a significant amount of unclassified pixels of 7.43% in the 0.1 threshold image. The classified images C present equal proportions of carbonate mineral mixtures for both threshold angles, which are dominated by abundant 100D of 69.12%. The abundance images D for both threshold angles contain mainly abundant 25C-75D of around 39%.

3.1.3. LSU Classification Results

Figure 8a,c shows LSU classification images of the selected SisuCHEMA data using the laboratory endmembers of pure carbonate synthetic samples [38] as the reference spectra and unconstrained and constrained unmixing algorithms. The LSU images show variations of spatial distribution and abundance of carbonate mineral mixtures between unconstrained and constrained unmixing algorithms. The small abundant 100C in the images B and D is roughly classified by those unmixing methods with different proportions. The LSU results also exhibit a number of unclassified pixels (black pixels, Figure 8a,c). In this case, pixels having values above 1.0 or below 0.0 consider as the unclassified pixels.

Figure 8. LSU classification results: (**a**) unconstrained dolomite endmember images, (**b**) estimated proportion of classified minerals derived from the unconstrained images, (**c**) constrained dolomite endmember images using a 1.0 default value of weight, and (**d**) estimated proportion of classified minerals derived from the constrained images. The classification images present a slight variability of carbonate fractional abundances in different unmixing approaches. (C = calcite and D = dolomite, prefix numbers showing the mineral contents in percent).

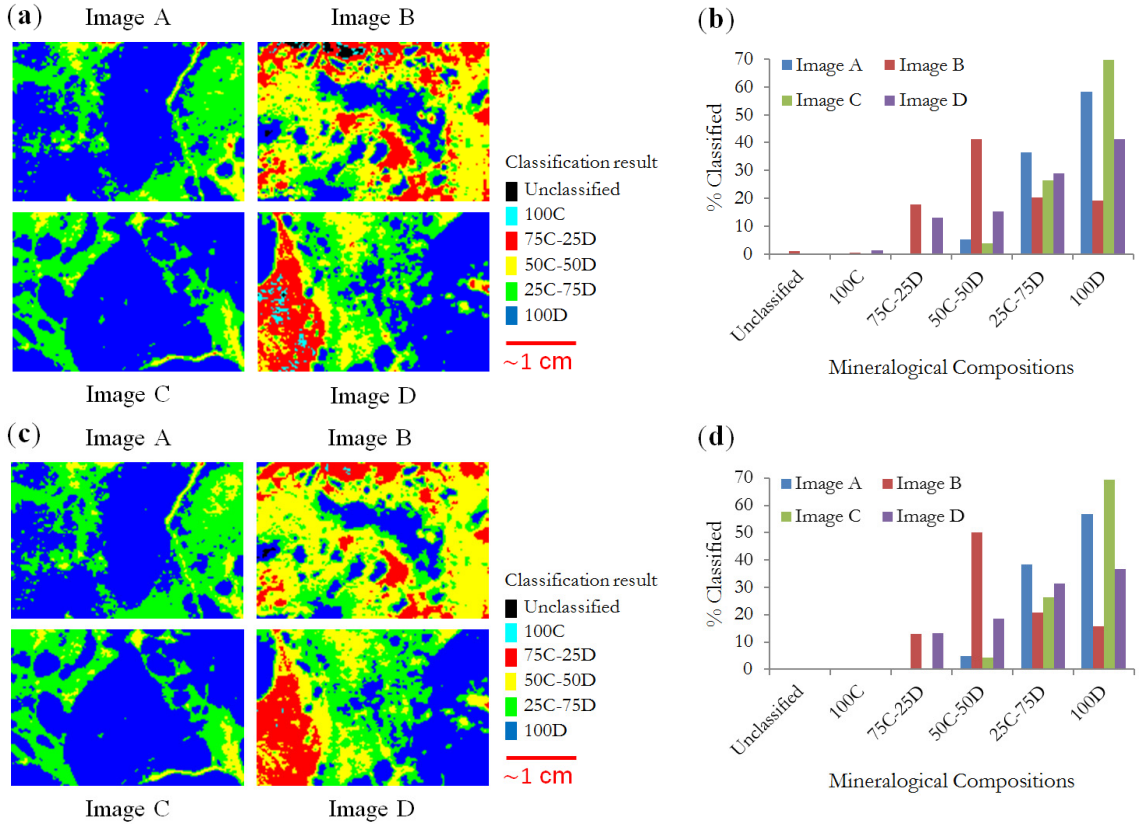

The estimation of relative mineral abundances of the carbonate samples derived from the unconstrained and constrained dolomite endmember images is shown in Figure 8b,d. The abundance images A are dominated by abundant 100D with a slight different proportion which is of 58.18% in the unconstrained image and 56.78% in the constrained image. The unconstrained image B shows relatively similar proportions of carbonate mineral mixtures as the constrained image B. These classified images are dominated by carbonate abundances of 50C-50D, but the proportions of this carbonate mineral are about 9% higher in the constrained image than the unconstrained image. The unconstrained and constrained images C classify the same dominant mineral abundance, which is abundant 100D of around 69%. However, the small proportion of abundant 75C-25D (Red pixels, Figure 8c) is unclassified in the constrained image C. The unconstrained and constrained images D are constituted mainly by abundant 100D and abundant 25C-75D, whereas the proportions of abundant 100D are around 5% higher in the unconstrained image than the constrained image. In addition, although both unmixing algorithms identify the presence of small abundant 100C in the images D, these approaches estimate the abundant 100C in different proportions, which are 1.41% for the unconstrained image and 0.04% for the constrained image.

Figure 9. Histograms comparing proportion estimation of carbonate mineral mixtures of three spectral analysis techniques applied to the selected SisuCHEMA images. Samples (**a**) A, (**b**) B, (**c**) C, and (**d**) D. Classification results of carbonate mineral abundances differ slightly from one approach to another for a given image.

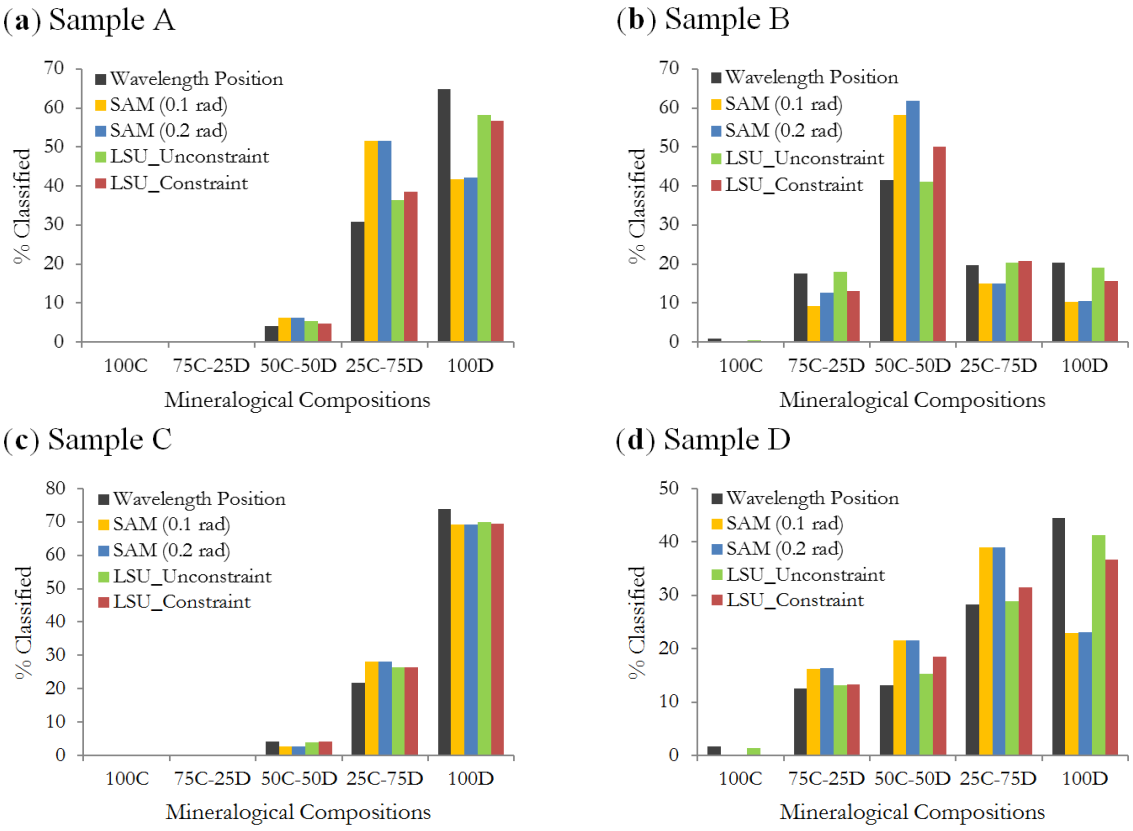

3.1.4. Comparison of the Image Classification Approaches

Figure 9 shows comparison of the relative estimated abundance of carbonate mineral mixtures on the rock samples derived from the classified images (Figures 6a, 7a,c and 8a,c) by applying various spectral recognition methods. It shows that the proportion estimation of these minerals varies between the spectral classification approaches (Figure 9), but overall the classified mineral distributions on the rock samples are almost at the same general areas (Figures 6a, 7a,c and 8a,c).

Table 2. Confusion matrix of the classified carbonate mineral mixtures by comparing spectral angle mapper (SAM) and linear spectral unmixing (LSU) results with wavelength position results. Samples (**a**) A, (**b**) B, (**c**) C, and (**d**) D. (C = calcite and D = dolomite, prefix numbers showing the mineral contents in percent).

(a) Sample A

SAM (0.1 rad)

	100C	75C-25D	50C-50D	25C-75D	100D
100C	0	0	0	0	0
75C-25D	0	30.77	0	0	0
50C-50D	0	69.23	68.82	10.26	0.34
25C-75D	0	0	24.12	71.35	44.40
100D	0	0	7.07	18.39	55.26
Overall classification accuracy: 60.74%					

LSU (Unconstraint)

	100C	75C-25D	50C-50D	25C-75D	100D
100C	0	0	0	0	0
75C-25D	0	53.85	2.58	0.02	0
50C-50D	0	30.77	37.84	8.84	1.50
25C-75D	0	15.38	57.60	59.20	24.18
100D	0	0	1.98	31.94	74.32
Overall classification accuracy: 68.12%					

SAM (0.2 rad)

	100C	75C-25D	50C-50D	25C-75D	100D
100C	0	0	0	0	0
75C-25D	0	30.77	0	0	0.01
50C-50D	0	69.23	68.09	10.20	0.34
25C-75D	0	0	23.86	70.90	44.31
100D	0	0	8.05	18.90	55.34
Overall classification accuracy: 60.64%					

LSU (Constraint)

	100C	75C-25D	50C-50D	25C-75D	100D
100C	0	0	0	0	0
75C-25D	0	15.38	0.15	0	0
50C-50D	0	76.92	53.50	6.70	0.58
25C-75D	0	7.69	45.14	64.27	25.84
100D	0	0	1.22	29.03	73.58
Overall classification accuracy: 69.83%					

(b) Sample B

SAM (0.1 rad)

	100C	75C-25D	50C-50D	25C-75D	100D
100C	0	0	0	0	0
75C-25D	96.00	54.57	4.78	0.03	0
50C-50D	4.00	45.43	93.20	71.48	6.22
25C-75D	0	0	2.00	25.81	45.10
100D	0	0	0.02	2.67	48.68
Overall classification accuracy: 63.47%					

LSU (Unconstraint)

	100C	75C-25D	50C-50D	25C-75D	100D
100C	5.60	2.65	0.02	0	0
75C-25D	88.80	66.41	14.16	0.93	0.09
50C-50D	4.80	30.36	68.33	36.78	2.36
25C-75D	0.80	0.57	16.47	45.45	21.61
100D	0	0	1.03	16.83	75.93
Overall classification accuracy: 64.49%					

SAM (0.2 rad)

	100C	75C-25D	50C-50D	25C-75D	100D
100C	0	0	0	0	0
75C-25D	94.04	55.54	4.94	0.03	0
50C-50D	5.96	44.46	93.10	71.44	6.16
25C-75D	0	0	1.93	25.73	44.68
100D	0	0	0.03	2.79	49.16
Overall classification accuracy: 63.41%					

LSU (Constraint)

	100C	75C-25D	50C-50D	25C-75D	100D
100C	4.58	0.40	0	0	0
75C-25D	90.20	56.93	5.23	0.19	0
50C-50D	4.58	42.57	82.02	41.28	2.43
25C-75D	0.65	0.11	12.65	51.43	26.76
100D	0	0	0.09	7.10	70.81
Overall classification accuracy: 68.55%					

Table 2. *Cont.*

(c) Sample C

SAM (0.1 rad)

	100C	75C-25D	50C-50D	25C-75D	100D
100C	0	0	0	0	0
75C-25D	0	50.00	0.31	0	0
50C-50D	0	50.00	35.31	5.03	0.10
25C-75D	0	0	59.84	74.67	12.70
100D	0	0	4.53	20.31	87.20
Overall classification accuracy: 82.31%					

LSU (Unconstraint)

	100C	75C-25D	50C-50D	25C-75D	100D
100C	0	0	0	0	0
75C-25D	0	0	0.31	0.03	0
50C-50D	0	68.42	41.88	8.37	0.30
25C-75D	0	31.58	56.25	71.99	11.16
100D	0	0	1.56	19.61	88.54
Overall classification accuracy: 82.92%					

SAM (0.2 rad)

	100C	75C-25D	50C-50D	25C-75D	100D
100C	0	0	0	0	0
75C-25D	0	47.37	0.31	0	0
50C-50D	0	47.37	35.31	5.03	0.10
25C-75D	0	0	59.84	74.67	12.70
100D	0	5.26	4.53	20.31	87.20
Overall classification accuracy: 82.31%					

LSU (Constraint)

	100C	75C-25D	50C-50D	25C-75D	100D
100C	0	0	0	0	0
75C-25D	0	0	0	0	0
50C-50D	0	94.74	48.13	8.92	0.22
25C-75D	0	5.26	50.94	73.47	11.30
100D	0	0	0.94	17.61	88.48
Overall classification accuracy: 83.45%					

(d) Sample D

SAM (0.1 rad)

	100C	75C-25D	50C-50D	25C-75D	100D
100C	0	0	0	0	0
75C-25D	100	95.32	21.11	0.09	0
50C-50D	0	4.68	66.41	38.03	3.66
25C-75D	0	0	12.34	59.20	46.50
100D	0	0	0.15	2.68	49.84
Overall classification accuracy: 59.48%					

LSU (Unconstraint)

	100C	75C-25D	50C-50D	25C-75D	100D
100C	26.25	7.73	0.10	0	0
75C-25D	61.78	78.03	17.34	0.16	0
50C-50D	11.97	13.99	50.75	20.27	2.25
25C-75D	0	0.25	30.94	58.11	18.69
100D	0	0	0.87	21.46	79.06
Overall classification accuracy: 68.43%					

SAM (0.2 rad)

	100C	75C-25D	50C-50D	25C-75D	100D
100C	0	0	0	0	0
75C-25D	100	95.28	21.16	0.11	0
50C-50D	0	4.72	66.30	37.93	3.65
25C-75D	0	0	12.35	59.06	46.45
100D	0	0	0.19	2.90	49.89
Overall classification accuracy: 59.48%					

LSU (Constraint)

	100C	75C-25D	50C-50D	25C-75D	100D
100C	0.77	0.20	0	0	0
75C-25D	91.19	82.19	11.14	0	0
50C-50D	8.05	17.61	65.57	23.55	2.17
25C-75D	0	0	23.00	62.70	24.28
100D	0	0	0.29	13.75	73.55
Overall classification accuracy: 69.31%					

The wavelength position analysis approach of the SisuCHEMA image spectra well characterizes the carbonate mineral mixtures and estimates the proportions of these carbonate minerals on the rock surfaces. In comparison to the wavelength position classifier, the SAM and LSU algorithms tend to produce some misclassified and unclassified pixels of carbonate mineral mixtures (Figures 7a,c and 8a,c). The small abundant 100C in the images B and D (Figure 7a,c) is to be unclassified by the SAM algorithm. These small proportions of unclassified pixels from the SAM and LSU results are excluded from comparison of the classification methods. Hence, we only consider and analyze the proportions

of five carbonate mineral mixtures consisted of 100C, 75C-25D, 50C-50D, 25C-75D, and 100D for comparison and accuracy assessment of these classification methods.

The proportions of carbonate mineral mixtures of 25C-75D and 100D estimated from the SAM results of images A differ approximately 21% and 23% from the wavelength position classification result, respectively (Figure 9a). The proportion differences of these carbonate compositions in images A result in around 6% for the unconstrained and 8% for constrained LSU methods, as compared to the wavelength position result (Figure 9a). The resulting proportion of 50C-50D from the SAM results of images B differs roughly 17% from the wavelength position result, and the unconstrained and constrained LSU results exhibit a difference of 0.30% and 8.67%, respectively (Figure 9b). The proportions of carbonate mineral mixtures derived from the SAM and LSU results of images C are nearly the same as the wavelength position result (Figure 9c). SAM classification results of images D illustrate that the proportions of 25C-75D and 100D differ approximately 11% and 21% from the wavelength position result, respectively, while the proportion differences of these compositions in images D result in less than 3% for the unconstrained and 7% for constrained LSU methods (Figure 9d).

The overall classification accuracies of carbonate mineral mixtures using these spectral analysis approaches are illustrated in Table 2. The results show that the classification accuracies of LSU images are slightly higher than SAM images when compared with wavelength position images. The classification accuracies of SAM results are almost the same for both threshold angles. It also indicates that the classification accuracies of constrained LSU results improve above 1% for images A and B and above 0.5% for images C and D when compared with unconstrained LSU results. The classification accuracies of the carbonate mixtures in image C using these spectral methods are around 80%, while the other classified images (images A, B, and D) show an overall accuracy around 60%.

3.2. PXRF Geochemical Analysis Results

Geochemical analysis of elements on the selected carbonate rock samples using a PXRF over two spot measurements for each sample is shown in Table 1. The PXRF laboratory analysis result shows that the samples contain mineralogical associations of major elements, such as Ca and Mg and trace elements such as Ba, Fe, Al, Si, Cl, and S (Table 1). Element concentrations of Sr and Ti are mostly less than 30 ppm and 55 ppm, respectively. These major and trace elements indicate that the rock samples are dominated by carbonate minerals with various compositions of mineral mixtures. Low concentrations of the trace elements such as Fe, Al, Si, and S (Table 1) give possibly an indication of iron oxide, clay and sulfate mineral associations in the carbonate rocks.

It can also be seen on the correlation between major elemental concentrations and average spectral classification results (Figure 10) derived from the regions of interest (ROIs) of the classified images (Figures 6a, 7a and 8a) over the same areas as PXRF spot measurements (Figure 3). As illustrated in Figure 10a, an approximate linear relationship is observed between chemical contents and average wavelength positions of the classified images. However, some relationships between chemical contents and average spectral angles of SAM and fraction values of LSU are poorer than the former for both 100C and 100D images (Figure 10b,c and Table 3). Although there is a well-fitted correlation of Ca content with average mineral spectral parameters, this relation becomes a relatively weak with Mg content in the samples.

The average band positions shift towards longer wavelength in the SWIR region with increasing Ca content, but the average band positions shift towards shorter wavelength in the SWIR with increasing Mg content (Figure 10a). It reveals that the wavelength positions depend on Ca and Mg contents in the samples. Definite patterns are not observed between the spectral angles of 100D rule images and Ca and Mg contents (Figure 10b). The average dolomite abundances (fraction values) of the unconstrained unmixing 100D images decrease with increasing Ca content and vice versa for Mg content (Figure 10c). It indicates that higher fractions represent the dominancy of dolomite, which is related to increasing Mg content in the samples.

Figure 10. Correlation between major geochemical elements in the carbonate samples and the average of spectral parameter results of the classified images. Physical model relating Ca and Mg contents in the carbonate samples and spectral parameters derived from images classified by (**a**) wavelength position analysis, (**b**) and (**c**) SAM and unconstrained LSU methods for 100D images, respectively. These average spectral classification results were acquired on the same regions of interest (ROIs) of the PXRF spot measurements.

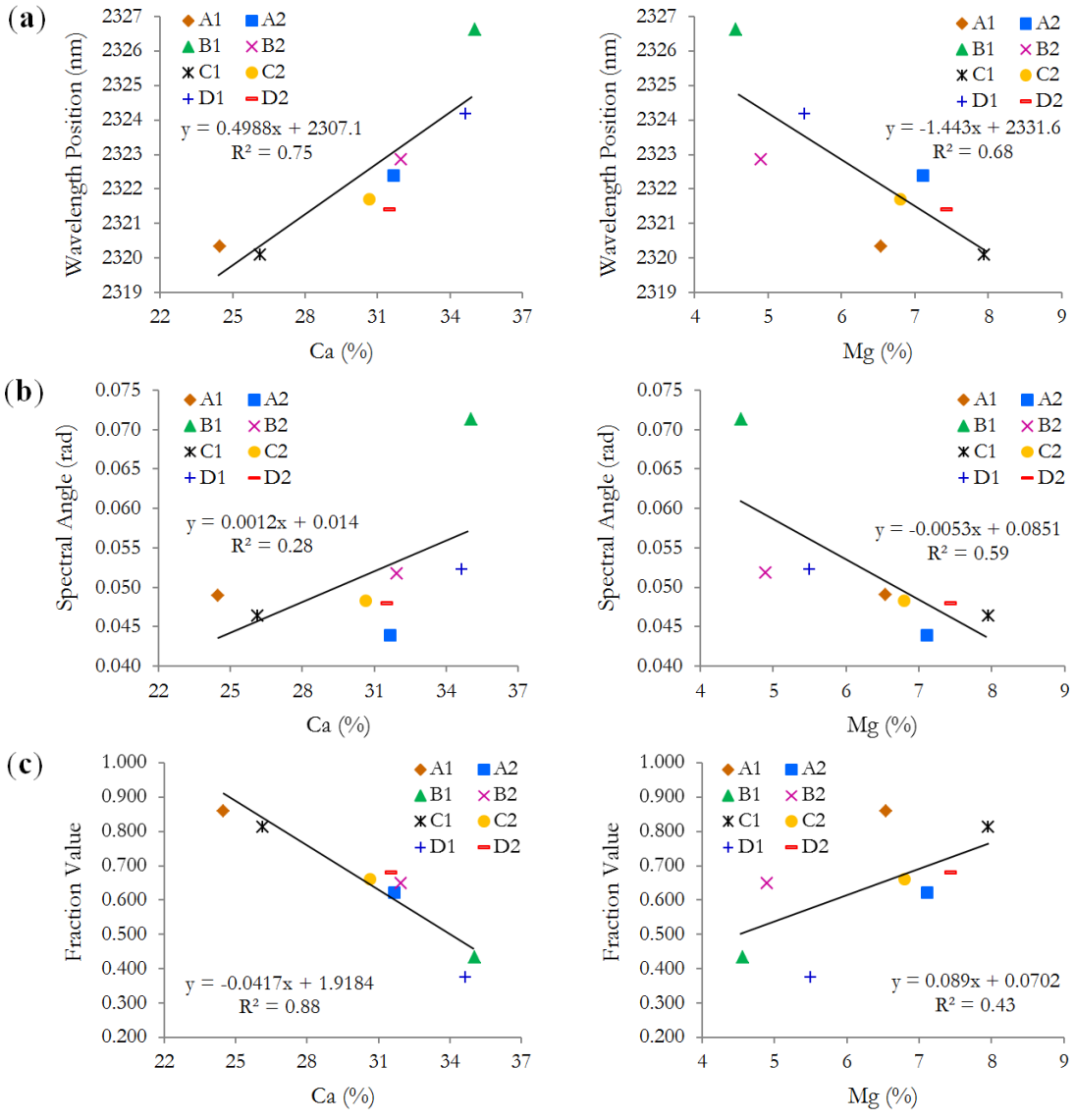

Table 3. Summary of the linear regression results from SAM and LSU classifications of images on the major geochemical elements (Ca and Mg) in carbonate samples. Note that the average spectral classification results were acquired on the same regions of interest (ROIs) of the PXRF spot measurements.

Spectral Parameters	Classification Methods	Classified Images	Geochemical Parameters			
			Ca		Mg	
			R^2	Regression Equation	R^2	Regression Equation
Spectral angle	SAM (0.1 rad)	100C	0.88	y = −0.0031x + 0.1795	0.44	y = 0.0066x + 0.0417
Fraction value	LSU-Unconstraint	100C	0.70	y = 0.0231x − 0.4855	0.64	y = −0.0674x + 0.6541
Fraction value	LSU-Constraint	100C	0.54	y = 0.0196x − 0.4041	0.61	y = −0.0634x + 0.6026
Fraction value	LSU-Constraint	100D	0.91	y = −0.037x + 1.8083	0.50	y = 0.0835x + 0.1404

4. Discussion

Results of this study indicated that differences in carbonate mineral mixtures identification and proportion estimation of these minerals of the rock samples depend on spectral classification approaches, user-selected parameters, and match between reference spectra and image spectra (Figure 9). However, the overall spatial distribution of carbonate mineral mixtures classified by the three spectral analysis approaches (Figures 6a, 7a,c and 8a,c) has nearly the same pattern on the rock surfaces. Geochemical results analysis also demonstrated a high correlation between chemical contents and spectroscopic results, proving various compositional mineral mixtures identification in the samples (Figure 10 and Table 3).

The absorption wavelength position analysis approach is sensitive to slight changes of carbonate minerals composition, even in areas with "noisier" spectral responses. The accurate determination of wavelength position improves by applying a polynomial fit to the continuum-removed spectra [20,23]. It should be noted that absorption features of the SWIR carbonate spectra may be affected by the result of varying grain sizes [8,37–39], weathering, and mixing with organic matters forming a coating on carbonate particles [37,39] and iron [8,37] in carbonate samples. Nevertheless, the wavelength position approach can identify carbonate mineral mixtures based on spectral characteristics. Thus, occurrence of prominent absorption feature in the SWIR spectra around 2300–2350 nm due to vibrational processes of the carbonate ions (CO_3^{2-}) [8,32,34,37] can be used to distinguish carbonate mineral mixtures in the rock samples [8,32,34,37,38]. The band positions of both pure and mixed calcite and dolomite are centered within the range of carbonate wavelength positions observed in previous studies [8,32,34,37,38]. The carbonate mixture band positions are determined by the quantity of calcite and dolomite in the samples [37,38].

The outcome of SAM and LSU classification methods demonstrates a number of misclassified and unclassified pixels of carbonate mineral mixtures (Figures 7 and 8), as compared to wavelength position approach (Figure 6). This may contribute to the difficulty in proportion estimation of carbonate mineral mixtures on the rock surfaces (Figure 9). Most probably it could be due to the spectral shape similarities of endmembers used for classification (Figure 5) or omitted endmember from analysis and mismatches between spectral endmembers and spectra of image pixels. As depicted in Table 2, the overall classification accuracies of LSU images are slightly higher than SAM images. SAM algorithms were relatively poor in accuracy to discriminate carbonate mineral mixtures between 100D

and 25C-75D and between 100C and 75C-25D. These misclassifications may be influenced by very similar shape of the endmember spectra although their band positions of absorption features are centered at a slightly different wavelength. Previous studies have also described that SAM algorithm is not searching for diagnostic mineral absorption features, but it depends on average match of the entire reference spectra [28,29] and it is insensitive to illumination and albedo differences [27–29,31].

Furthermore, despite the fact that the shape of spectral endmembers of pure calcite and dolomite is similar to each other with a slight shift absorption band position, the unconstrained and constrained LSU algorithms provide a good agreement in carbonate mineral mixtures identification on the selected SisuCHEMA images. It indicated that the unknown spectrum at each pixel of the images may be formed by a linear combination of the reference spectrum or endmember. The results of linear unmixing processes depend on the combination of the correlation between spectral minerals forming the mixture and the endmembers used in analysis [5,45]. Generally the LSU algorithms show a relative similar mineral mixtures distribution and proportion estimation of carbonate compositions to wavelength position approach. The constrained LSU results achieved slightly higher classification accuracies than the unconstrained LSU results, by comparing with wavelength position results. The differences in overall classification accuracy may be linked to more unclassified pixels in the unconstrained results, particularly in the images B and D (Figure 8a). However, wavelength position analysis and LSU classification methods require knowledge of spectral mixture characteristics and further preprocessing of the data to estimate the proportion of the mixed minerals on the selected SisuCHEMA images.

The PXRF geochemical analysis results of the rock samples (Table 1) also confirm and prove the presence of carbonate mineral mixtures with various compositions. As the major element concentrations of Ca and Mg are lower than their stoichiometric values in pure calcite and dolomite. These major and trace elements can help to characterize mineralogic assemblages of carbonate rocks, which agree with results of previous studies [48–51]. The results from Figure 10 and Table 3 show that using the wavelength of minimum absorption through the wavelength position approach provides the best predictive value for inverting Ca and Mg chemistry to spectral parameters. Both the spectral angle (through SAM) and the fractional abundance (through LSU) overall performance is poorer than wavelength position approach. However, they showed acceptable results for individual chemical elements inversion. It should be noted that the LSU outperforms the SAM. This is attributed to the fact that the endmembers used are correlated and this works in favor of the LSU algorithm, which uses this dependency while the SAM assumes the endmembers are independent. In other words, in SAM endmembers are tested one at the time against pixel spectra, but in LSU all endmembers are used simultaneously in the inversion of the model. It can be envisaged that if the collinearity between the endmembers decreases by including more endmembers or less correlated endmembers [52] and this improves the performance of LSU over SAM although in the present study this could not be tested. As a result, the finding of this study could be implemented to determine naturally mixed minerals and estimate the proportions of minerals on rock surfaces using laboratory-based hyperspectral data, confirming results of previous studies [18–21].

5. Conclusions

This study for the first time presents the use of SisuCHEMA hyperspectral imagery to identify the chemical composition of naturally mixed minerals and estimate the relative mineral abundances in hand specimens of carbonate rocks. We demonstrate how to derive the chemical composition (Ca-Mg ratio) of carbonate minerals at a pixel (e.g., sub-grain) level using spectral analysis methods from the image pixel spectra. Classified images created using wavelength position, spectral angle mapper (SAM), and linear spectral unmixing (LSU) were used to spatially map calcite-dolomite mixtures with various carbonate mineral compositions and proportions. The wavelength position approach enables to determine all compositional variations of carbonate mineral mixtures in the rock samples when compared to the SAM and LSU approaches.

The relationship between major geochemical elements (Ca and Mg) and average spectral parameters (wavelength position, spectral angle of SAM, and fraction value of LSU) also proves the presence of various carbonate mixtures with different mineralogical compositions on the rock surfaces. Our study indicates that the wavelength position approach is a more stable, standardized and reproducible technique for determining the carbonate mineral chemistry from the image pixel spectra than the SAM and LSU methods. For future research, the established correlation between geochemical elements and wavelength position (physical models) can be used for inverse modeling of hyperspectral imagery in estimating the chemical composition of carbonate minerals on rock surfaces. In a practical sense, understanding of the carbonate mineral chemistry contributes to the developing a frame-work for the cement industry in assessing the purity and the chemical composition of carbonate minerals.

Acknowledgments

The authors are thankful to the Government of Aceh Province, Indonesia for funding this PhD research. We want to express our gratitude to Steven de Jong and teams for their help to collect carbonate rock samples and provide a geological overview of the samples, Boudewijn de Smeth for his assistance in sample preparations and PXRF geochemical analysis, Wim Bakker for HypPy software assistance and Frank van Ruitenbeek for discussions on the SWIR mineral spectra. The authors are also grateful to Abigail June Agus for her assisting in the SisuCHEMA hyperspectral data measurements. The authors would like to thank the anonymous reviewers for their very constructive comments and suggestions that have improved the quality of this paper.

Author Contributions

The designing, data processing, and analyzing of the study were conducted by Nasrullah Zaini. He wrote the draft of the manuscript. Freek van der Meer and Harald van der Werff assisted with the interpretation of the results and contributed to manuscript writing in all stages. All authors checked and revised the manuscript and contributed to the results.

Conflicts of Interest

The authors declare no conflict of interest.

References

1. Blatt, H.; Middleton, G.; Murray, R. Origin of Limestones. In *Origin of Sedimentary Rocks*; Prentice-Hall: Englewood Cliffs, NJ, USA, 1972; pp. 409–455.
2. Pettijohn, F.J. Limestones and Dolomite. In *Sedimentary Rocks*, 3rd ed.; Harper & Row: New York, NY, USA, 1975; pp. 316–391.
3. Mustard, J.F.; Pieters, C.M. Quantitative abundance estimates from bidirectional reflectance measurements. *J. Geophys. Res.* **1987**, *92*, E617–E626.
4. Clark, R.N. Spectroscopy of Rocks and Minerals, and Principles of Spectroscopy. In *Remote Sensing for the Earth Sciences: Manual of Remote Sensing*, 3rd ed.; Rencz, A.N., Ed.; John Wiley and Sons: New York, NY, USA, 1999; Volume 3, pp. 3–58.
5. Kruse, F.A.; Lefkoff, A.B.; Dietz, J.B. Expert system-based mineral mapping in Northern Death-Valley, California Nevada, using the airborne visible infrared imaging spectrometer (AVIRIS). *Remote Sens. Environ.* **1993**, *44*, 309–336.
6. Bishop, J.L.; Schelble, R.T.; McKay, C.P.; Brown, A.J.; Perry, K.A. Carbonate rocks in the Mojave Desert as an analogue for Martian carbonates. *Int. J. Astrobiol.* **2011**, *10*, 349–358.
7. Kaplan, M.Y.; Eren, M.; Kadir, S.; Kapur, S. Mineralogical, geochemical and isotopic characteristics of quaternary calcretes in the Adana region, Southern Turkey: Implications on their origin. *Catena* **2013**, *101*, 164–177.
8. Gaffey, S.J. Spectral reflectance of carbonate minerals in the visible and near infrared (0.35–2.55 microns): Calcite, aragonite, and dolomite. *Am. Mineralogist* **1986**, *71*, 151–162.
9. Sepulcre, S.; Durand, N.; Bard, E. Mineralogical determination of reef and periplatform carbonates: Calibration and implications for paleoceanography and radiochronology. *Global Planet Chang.* **2009**, *66*, 1–9.
10. Lein, A.Y. Authigenic carbonate formation in the ocean. *Lithol. Miner. Resour.* **2004**, *39*, 1–30.
11. Forbes, M.; Vogwill, R.; Onton, K. A characterisation of the coastal tufa deposits of south-west Western Australia. *Sediment. Geol.* **2010**, *232*, 52–65.
12. Vincent, B.; Fleury, M.; Santerre, Y.; Brigaud, B. NMR relaxation of neritic carbonates: An integrated petrophysical and petrographical approach. *J. Appl. Geophys.* **2011**, *74*, 38–58.
13. Dickson, J.A.D. A modified staining technique for carbonates in thin section. *Nature* **1965**, *205*, 587–587.
14. Friedman, G.M. Identification of carbonate minerals by staining methods. *J. Sediment. Res.* **1959**, *29*, 87–97.
15. Hitzman, M.W. Routine staining of drill core to determine carbonate mineralogy and distinguish carbonate alteration textures. *Miner. Deposita* **1999**, *34*, 794–798.
16. Kato, K.; Wada, H.; Fujioka, K. The application of chemical staining to separate calcite and aragonite minerals for micro-scale isotopic analyses. *Geochem. J.* **2003**, *37*, 291–297.
17. Specim. Available online: http://www.specim.fi/index.php/products/geology/sisuchema/ (accessed on 19 October 2010).

18. Baissa, R.; Labbassi, K.; Launeau, P.; Gaudin, A.; Ouajhain, B. Using HySpex SWIR-320m hyperspectral data for the identification and mapping of minerals in hand specimens of carbonate rocks from the Ankloute Formation (Agadir Basin, Western Morocco). *J. Afr. Earth Sci.* **2011**, *61*, 1–9.
19. Haest, M.; Cudahy, T.; Laukamp, C.; Gregory, S. Quantitative mineralogy from infrared spectroscopic data. I. Validation of mineral abundance and composition scripts at the Rocklea channel iron deposit in Western Australia. *Econ. Geol.* **2012**, *107*, 209–228.
20. Murphy, R.J.; Schneider, S.; Monteiro, S.T. Consistency of measurements of wavelength position from hyperspectral imagery: Use of the ferric iron crystal field absorption at 900 nm as an indicator of mineralogy. *IEEE Trans. Geosci. Remote Sens.* **2014**, *52*, 2843–2857.
21. Haest, M.; Cudahy, T.; Laukamp, C.; Gregory, S. Quantitative mineralogy from infrared spectroscopic data. II. Three-dimensional mineralogical characterization of the Rocklea channel iron deposit, Western Australia. *Econ. Geol.* **2012**, *107*, 229–249.
22. Clark, R.N.; Roush, T.L. Reflectance spectroscopy-quantitative analysis techniques for remote sensing applications. *J. Geophys. Res.* **1984**, *89*, 6329–6340.
23. Rodger, A.; Laukamp, C.; Haest, M.; Cudahy, T. A simple quadratic method of absorption feature wavelength estimation in continuum removed spectra. *Remote Sens. Environ.* **2012**, *118*, 273–283.
24. Kruse, F.A.; Lefkoff, A.B.; Boardman, J.W.; Heidebrecht, K.B.; Shapiro, A.T.; Barloon, P.J.; Goetz, A.F.H. The spectral image processing system (SIPS)—Interactive visualization and analysis of imaging spectrometer data. *Remote Sens. Environ.* **1993**, *44*, 145–163.
25. Boardman, J.W. Inversion of Imaging Spectrometry Data Using Singular Value Decomposition. In Proceedings of 12th Canadian Symposium on Remote Sensing IGARSS'89, Vancouver, Canada, 13 July 1989; pp. 2069–2072.
26. Adams, J.B.; Smith, M.O.; Gillespie, A.R. Imaging Spectroscopy: Interpretation Based on Spectral Mixture Analysis. In *Remote Geochemical Analysis: Elemental and Mineralogical Composition*; Pieters, C.M.; Englert, P.A.J., Eds.; Cambridge University Press: New York, NY, USA, 1993; pp. 145–166.
27. Murphy, R.J.; Monteiro, S.T.; Schneider, S. Evaluating classification techniques for mapping vertical geology using field-based hyperspectral sensors. *IEEE Trans. Geosci. Remote Sens.* **2012**, *50*, 3066–3080.
28. van der Meer, F. The effectiveness of spectral similarity measures for the analysis of hyperspectral imagery. *Int. J. Appl. Earth Obs. Geoinf.* **2006**, *8*, 3–17.
29. Hecker, C.; van der Meijde, M.; van der Werff, H.; van der Meer, F.D. Assessing the influence of reference spectra on synthetic SAM classification results. *IEEE Trans. Geosci. Remote Sens.* **2008**, *46*, 4162–4172.
30. Riaza, A.; Muller, A. Hyperspectral remote sensing monitoring of pyrite mine wastes: A record of climate variability (Pyrite Belt, Spain). *Environ. Earth Sci.* **2010**, *61*, 575–594.
31. Aspinall, R.J.; Marcus, W.A.; Boardman, J.W. Considerations in collecting, processing, and analysing high spatial resolution hyperspectral data for environmental investigations. *J. Geograph. Syst.* **2002**, *4*, 15–29.
32. Hunt, G.R.; Salisbury, J.W. Visible and near infrared spectra of minerals and rocks: II. Carbonates. *Mod. Geol.* **1971**, *2*, 23–30.

33. Hunt, G.R. Spectral signatures of particulate minerals in the visible and near infrared. *Geophysics* **1977**, *42*, 501–513.
34. Clark, R.N.; King, T.V.V.; Klejwa, M.; Swayze, G.A.; Vergo, N. High spectral resolution reflectance spectroscopy of minerals. *J. Geophys. Res.* **1990**, *95*, 12653–12680.
35. Hunt, G.R.; Salisbury, J.W. Visible and near-infrared spectra of minerals and rocks: I. Silicate minerals. *Mod. Geol.* **1970**, *1*, 283–300.
36. Povarennykh, A.S. Use of infrared-spectra for determination of minerals. *Am. Mineralogist* **1978**, *63*, 956–959.
37. Van der Meer, F.D. Spectral reflectance of carbonate mineral mixtures and bidirectional reflectance theory: Quantitative analysis techniques for application in remote sensing. *Remote Sens. Rev.* **1995**, *13*, 67–94.
38. Zaini, N.; van der Meer, F.; van der Werff, H. Effect of grain size and mineral mixing on carbonate absorption features in the SWIR and TIR wavelength regions. *Remote Sens.* **2012**, *4*, 987–1003.
39. Crowley, J.K. Visible and near-infrared spectra of carbonate rocks-reflectance variations related to petrographic texture and impurities. *J. Geophys. Res.: Solid Earth* **1986**, *91*, 5001–5012.
40. Kurz, T.H.; Dewit, J.; Buckley, S.J.; Thurmond, J.B.; Hunt, D.W.; Swennen, R. Hyperspectral image analysis of different carbonate lithologies (limestone, karst and hydrothermal dolomites): the Pozalagua Quarry case study (Cantabria, North-West Spain). *Sedimentology* **2012**, *59*, 623–645.
41. Agus, A.J.L. Mapping White Mica in Milled Porphyry Copper Pebbles Using Hyperspectral Imagery: An Exploratory Study. Master's Thesis, University of Twente, Enschede, The Netherlands, 2011.
42. Bogdanoff, S.; Donnot, M.; Ellenberger, F. *Carte Geologique de la France à 1 :50.000 et Notice Explicative, Feuille Bedarieux*; In Edition du BRGM: Orléans, France, 1984.
43. ITT. *Visual Information Solutions*. Available online: http://www.ittvis.com (accessed on 18 May 2010).
44. Thermo Scientific. *Thermo Fisher Scientific Niton XL3 Analyzer User's Guide*, Version 7.0.1; Thermo Fisher Scientific Inc.: Munich, Germany, 2010.
45. van der Meer, F.; de Jong, S.M. Improving the results of spectral unmixing of Landsat Thematic Mapper imagery by enhancing the orthogonality of end-members. *Int. J. Remote Sens.* **2000**, *21*, 2781–2797.
46. Bakker, W. *HypPy User Manual: Graphical User-Interface (GUI)*, Version 2.6; ITC: Enschede, The Netherlands, 2012.
47. Settle, J.J.; Drake, N.A. Linear mixing and the estimation of ground cover proportions. *Int. J. Remote Sens.* **1993**, *14*, 1159–1177.
48. Barber, C. Major and trace element associations in limestones and dolomites. *Chem. Geol.* **1974**, *14*, 273–280.
49. Robinson, P. Determination of calcium, magnesium, manganese, strontium, sodium, and iron in the carbonate fraction of limestones and dolomites. *Chem. Geol.* **1980**, *28*, 135–146.
50. Thompson, G.; Bankston, D.C.; Pasley, S.M. Trace element data for reference carbonate rocks. *Chem. Geol.* **1970**, *6*, 165–170.

51. Wolf, K.H.; Chilingar, G.V.; Beales, F.W. Elemental Composition of Carbonate Skeletons, Minerals, and Sediments. In *Carbonate Rocks: Physical and Chemical Aspects*; Chilingar, G.V., Bissell, H.J., Fairbridge, R.W., Eds.; Elsevier: Amsterdam, The Netherlands, 1967; Volume 9B, pp. 23–150.
52. Van der Meer, F.D.; Jia, X.P. Collinearity and orthogonality of endmembers in linear spectral unmixing. *Int. J. Appl. Earth Obs. Geoinf.* **2012**, *18*, 491–503.